Vorticity Equation Solutions for Slender Wings at High Incidence

A. Dagan*
RAFAEL, Haifa, Israel
and
D. Almosnino†
RAFAEL and Technion—Israel Institute of Technology, Haifa, Israel

A new approximate model for the viscous flow around slender wing or body shapes at high angles of attack is presented. The present theory assumes that the flow over a slender shape can be divided into an inner, viscous part that is described by the vorticity equation and a matching outer potential part. At present, incompressible flow conditions are assumed. The parabolization of the problem that results from these assumptions allows one to obtain a fast plane-marching solution scheme. The analysis shows that the Sychev geometric similarity parameter applies to the present viscous flow model and not only to the inviscid models. The present theory supports the implusive start flow analogy. In the particular case of slender delta wings, the present theory yields expressions similar to those of the Polhamus suction analogy for the lift coefficient. The feasibility of the present method is tested on a number of delta wings with flat elliptical cross sections, using several Sychev similarity parameters at Reynolds numbers of $O(10^5)$ based on the wing root chord and the freestream velocity. Results include aerodynamic coefficients, surface pressure distributions, and velocity field as well as vorticity contours in crossflow planes. Very good agreement is obtained between the calculated aerodynamic coefficients and experimental data.

Introduction

HIGH angle of attack, subsonic flow calculations of slender wings and bodies that include separated vortex flow regions are one of the main challenges of present computational fluid dynamics (CFD) methods. Computational methods based on potential flow assumptions have been used extensively since the early days of modern computers to approximate separated vortex flows. These methods yield acceptable engineering results as long as the separation is well defined and not sensitive to viscous effects, as in the case of a sharp leading edge of a slender delta wing. With the growing capacity and performance of computers, inviscid solutions for the Euler equations have become available. Euler solvers are also limited by the inviscid flow assumption. As a result, the process of vorticity generation and diffusion from a smooth surface is not well defined and the solution in such a case is shown to be controlled by the artificial viscosity introduced into the numerical scheme.[1-2] The inherent limitations of the inviscid flow models and the further increase in computer performance encouraged the development of numerical codes that solve viscous flow models. Within this framework, much progress has been achieved lately in solving fully developed vortex flows over slender wings, with the introduction of solvers to the full Navier-Stokes equations[3] and also to their thin-layer approximation.[3-4] In Refs. 5 and 6, the incompressible flowfield over a delta and double delta wing is solved by adding an artificial time derivative of the pressure to the continuity equation. Consequently, the derived set of equations is integrated like a conventional, parabolic time dependent set. A typical computation of a round-edge delta wing is reported to take about 37 μs per grid point per iteration on a CDC Cyber 205 machine, with 572,000 total number of grid points and 400 global iterations needed to solve the case. Ref. 1 solves the Navier-Stokes equations for a laminar compressible flow over round edge delta wings using the finite volume approach and a mesh of 411,000 points consuming 23 μs per grid point per time step on a similar machine (overall number of time steps not reported). A different class of solutions is available via the thin-layer approximation of Navier-Stokes equations, where the normal derivative in the diffusion term is retained. Such a method is used in Refs. 4 and 7 to solve similar cases using a mesh of 854,000 grid points, with typically 2000 global iterations that take 20 μs per grid point per iteration on a single processor Cray 2 machine or 8.6 μs on an Amdahl 1200, putting it in the same class as the previous two methods.

In view of these details, it seems that "the full Navier-Stokes solutions have not yet reached the stage at which the restrictions on computational speed and storage can be ignored."[3] It turns out that, in order to bridge over these computational restrictions, a relatively fast and reliable approximate viscous solution is needed, one that can be used as an engineering tool. The scope of such approximate solutions is to obtain relatively fast and satisfactory answers, usually sacrificing some accuracy and sometimes being limited in applicability to certain families of geometrical shapes (such as slender wings and bodies). The main efforts should be devoted in this context to reduce the number of global iterations and to store less data planes.

The Parabolized Navier-Stokes (PNS) method, for example, is widely used for computing steady-state solutions because by neglecting the derivatives of the streamwise diffusion terms, the reduced form resembles a set of parabolic equations in space. This method is very useful when dealing with supersonic flow, where the physical behavior of the equations becomes parabolic/hyperbolic. However the PNS method is almost as expensive as the full Navier-Stokes code when solving a subsonic flow regime. In that case, a global iteration method is still required to convey the elliptic behavior of the flowfield. Typically, such computations require several hundreds of global iterations to achieve convergence, depending on the

Received May 17, 1989; revision received Jan. 19, 1990.

*Research Scientist, Division 46. Member AIAA.
†Research Scientist, Division 46, and Adjunct Research Associate, Department of Aerospace Engineering. Member AIAA.

geometric shape.[8] This limitation is removed in Ref. 9 by deriving a nonelliptic set of equations that can be treated as an initial/boundary value problem, where only one global iteration is needed to obtain the solution in the subsonic case. This method yields satisfactory results for the inner flowfield in a duct and it encourages us to look for a similar approach to solve certain types of external flow problems.

The main motivation of the present study is to develop a fast and reliable approximate method to solve the subsonic vortical flow around slender configurations that can be used as an engineering tool. The present method is based on a new approximate model for the viscous flow around slender wings or body shapes at high angles of attack. The main assumption underlying the present theory is that the flow over a slender shape can be divided into an inner, viscous part that is described by the vorticity equation and a matching outer, potential part. The parabolization of the problem that results from these assumptions allows one to obtain a relatively fast plane-marching solution. One of the main features of the new model that emerges from the analysis is that the Sychev geometry similarity parameter[10] used by Refs. 11-13 within an inviscid slender wing or body model is also valid for the new viscous slender wing (or body) theory. Moreover, it transpires that for the first-order approximation, the inner, viscous flowfield generated by a slender configuration is of nonelliptic nature. The ellipticity of the physical phenomena is weakly introduced by the outer potential part of the flow, through the thickness effect of the body. The nonelliptic equations derived in the present theory reduce the amount of computational work. They do not require an intensive global iteration process, and the problem can be treated as an initial/boundary value problem.

At present the computations are for incompressible, steady flow solutions. However, the present theory can be extended to compressible as well as unsteady flows.

Theory

The vorticity generated along the leading edge of a slender wing is diffused and advected by the flow, generating a well-developed vortical region above the wing whose center may be defined by $r_v = O(z \cdot \tan\alpha)$(Fig. 1). Slenderness of both wing and vortex ($b_{max}/L \ll 1$) reduces the Navier-Stokes equations to the nondimensional form:

$$\lambda\left[\frac{\partial u}{\partial \tau} + w\frac{\partial u}{\partial z}\right] + u\frac{\partial u}{\partial x} + v\frac{\partial u}{\partial y} + \frac{\partial p}{\partial x} = \frac{1}{Re}\nabla^2 u \tag{1a}$$

$$\lambda\left[\frac{\partial v}{\partial \tau} + w\frac{\partial v}{\partial z}\right] + u\frac{\partial v}{\partial x} + v\frac{\partial v}{\partial y} + \frac{\partial p}{\partial y} = \frac{1}{Re}\nabla^2 v \tag{1b}$$

$$\lambda\left[\frac{\partial w}{\partial \tau} + w\frac{\partial w}{\partial z}\right] + u\frac{\partial w}{\partial x} + v\frac{\partial w}{\partial y} + \frac{\delta^2\partial p}{\lambda\,\partial z} = \frac{1}{Re}\nabla^2 w \tag{1c}$$

where $\tau = U_\infty t\cos\alpha/L$, and the crossflow velocities u,v are normalized by $U_\infty\sin\alpha$, whereas the axial velocity w is normalized by $U_\infty\cos\alpha$. The Reynolds number is defined as $Re = U_\infty b\sin\alpha/\nu$, and λ, known as the Sychev geometry similarity parameter, is defined as $\lambda = \delta/\tan\alpha$, where $\delta = \bar{b}/L$ (slenderness ratio). The coordinates x,y are scaled by $\bar{b} = b_{max}/2$, whereas z is normalized by L, and $\nabla^2 = \partial_x^2 + \partial_y^2$. Note that the definition of the Sychev parameter λ here is slightly different from that of Refs. 12 and 13. The system of Eqs. (1) describes the inner, viscous flow domain close to the wing including the leading-edge vortex. In this domain, the vorticity is generated and advected downstream. The solution of Eqs. (1) in this domain has to be matched to a potential flow solution in the outer flow domain (outer solution), where almost no vorticity exists. This matching will yield the necessary boundary condition for the pressure, introducing the elliptic behavior of the subsonic flowfield. Consequently, the set of Eqs. (1) with the proper boundary conditions that are found by the matching process determines the inner solution. In the absence of an axial pressure gradient, the system of Eqs. (1) is of nonelliptic nature,[9] making it attractive for PNS solvers. In the case of incompressible flow, it is convenient to introduce an equivalent set of equations using vorticity vector components as part of the variable system and retaining only first-order terms:

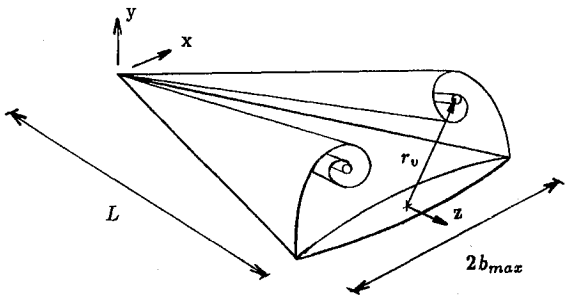

Fig. 1 Slender wing axes and notation.

$$\lambda\frac{\partial \Omega_z}{\partial \tau} + u_j\frac{\partial \Omega_z}{\partial x_j} = \frac{1}{Re}\nabla^2\Omega_z + \lambda\Omega_j\frac{\partial w}{\partial x_j} \tag{2a}$$

$$\lambda\frac{\partial w}{\partial \tau} + u_j\frac{\partial w}{\partial x_j} = \frac{1}{Re}\nabla^2 w \tag{2b}$$

$$\frac{\partial u_j}{\partial x_j} = 0 \tag{2c}$$

Here, $\Omega_j = (\Omega_x, \Omega_y, \Omega_z)$ is the vorticity vector, with $\Omega_z = \partial_x v - \partial_y u$ being its axial component, $\Omega_y = \partial_z u$ and $\Omega_x = -\partial_z v$, $u_j = (u, v, \lambda w)$ is the velocity vector; and $x_j = (x, y, z)$ is the vector of the coordinates. The third equation is the incompressible continuity equation. The crossflow velocity components can be defined using a vector potential notation:[3]

$$u = -\frac{\partial \psi}{\partial y} + \frac{\partial \phi}{\partial x} \tag{3a}$$

$$v = \frac{\partial \psi}{\partial x} + \frac{\partial \phi}{\partial y} \tag{3b}$$

Using this notation, the continuity equation together with the definition of Ω_z yield

$$\nabla^2\phi = -\lambda\frac{\partial w}{\partial z} \tag{4a}$$

$$\nabla^2\psi = \Omega_z \tag{4b}$$

On the solid surface, a no-slip condition is assumed, defining the boundary condition for ψ and ϕ. Since ψ represents the vortical area, the free constant of ψ can be chosen arbitrarily without violating the definition of the velocity (Eqs. 3). In this case, the free constant is chosen to be zero, where for large $r = \sqrt{x^2 + y^2}$, ψ is assumed to behave asymptotically as a multipole. Bearing in mind that the solution of the last set equations must match the far-field boundary condition, the resulting solution has the form of a potential source distribution along the z-axis, describing the thickness effect of the planform. This source term is analogous to the one obtained in the classical slender-body theory and it is described by

$$\lim_{r\to\infty}\phi = y + \frac{\lambda}{2\pi}\frac{\partial A}{\partial z}\ell n\, r + g(z) \tag{5}$$

where A is the cross-sectional area and $r = \sqrt{x^2 + y^2}$. The function $g(z)$ is obtained by matching the inner and the outer solutions, resulting in[14]

$$g(z) = \lambda\left\{\frac{\sigma(z)}{2\pi}\ell n\frac{\delta}{2} - \frac{1}{2\pi}\int_0^z \sigma(\xi)\ell n(z-\xi)d\xi + \frac{1}{2\pi}\int_z^1 \sigma(\xi)\ell n(\xi - z)d\xi - \frac{1}{2}\sigma(1)\ell n(1-z)\right\} \quad (6)$$

where $\sigma(z) = \partial_z A$. It is worth noting that no coupling exists between the free constant $g(z)$ of ϕ and the stream function of ψ for the first-order approximation.

The asymptotic behavior of the pressure distribution in the inner region is found to be

$$p\infty - p = 2\lambda\frac{\partial\phi}{\partial_z} + O(r^{-1}) \quad \text{for } r \to \infty \quad (7)$$

This expression can be used as the far-field pressure boundary condition.

Note that the chordwise free constant $g(z)$ introduces the elliptic influence of the outer potential flow, including the pressure term. For the first-order approximation, the free constant $g(z)$ is a function of the body thickness alone. The presence of the term $\ell n\delta$ breaks the similarity with respect to the Sychev parameter because the pressure distribution is weakly dependent on δ. However, this dependency does not enter the expressions for the lift or pitching moment coefficients (in a fashion similar to classical slender-body theory) since the pressure can be written as $p = p^* - p_0(z)$, where only p_0 depends on $g(z)$. In the present work, thickness effect is neglected, so $g(z)$ is zero. In some sense, this constant is equivalent to the free constant obtained by Ref. 9, when applying the global mass conservation principle.

The set of Eq. 1–5, together with the boundary conditions, completely determine the solution of a slender configuration at high angle of attack. The main advantage of this set of equations is its nonelliptic form. In other words, only one global iteration is required in order to obtain the solution because the problem can be treated as an initial/boundary value problem.[9] Another point of interest can be found in the fact that both lift and pitching moment coefficients are functions of the Sychev parameter as well as the crossflow Reynolds number. This fact essentially extends the applicability of Sychev similarity also to a smooth surface separation, making it subject for future studies.

One further simplification is made at this stage to facilitate a fast feasibility study of the method. The axial velocity component w decreases to zero within the thin layer zone, which is of order $O(Re^{-1/2})$, due to the non-slip boundary condition on the wing surface [see the axial momentum equations, Eqs. (1)]. Assuming that this happens only very close to the wing surface, the axial velocity component can be approximated as $w = 1 + O(\delta^2)$ throughout nearly all the field.[11] Using this simplification means neglecting the stretching mechanism of the vorticity described by the term $\Omega_j\partial_{x_j}w$ in Eqs. (2) and the source term $\partial_z w$ in Eqs. (4) in the thin boundary-layer zone. These terms contribute, in general, to the vorticity intensity (stretching mechanism) and reduce its viscous core (the source term). The last approximation is thus valid mainly for slender wings or bodies having a leading edge with small radius of curvature that strongly defines the primary separation of the flow. (This is equivalent to the definition of a Kutta point.) This approximation is also valid for a slender configuration at high angle of attack where $\lambda \ll 1$. In such a case, it can be shown [Eqs. (2)] that the effect of the stretching as well as the source term are small. It should be remembered that the present model of the flow still retains the diffusion terms in the crossflow plane, and so the mechanism of vorticity generation on the surface and its normal diffusion along the surface are retained as well. As a result, it is expected that a satisfactory description of the primary vortex can be obtained, with somewhat less accurate prediction of the secondary separation point.

Using the last approximation and rewriting the vorticity equation in Eqs. (2), using dimensional notation for convenient physical interpretation, results in Eq. (8):

$$\frac{\partial\Omega_z'}{\partial t} + U_\infty\cos\alpha\frac{\partial\Omega_z'}{\partial z'} + u'\frac{\partial\Omega_z'}{\partial x'} + v'\frac{\partial\Omega_z'}{\partial y'} = \nu\nabla^2_{x',y'}\Omega_z' \quad (8)$$

with the prime denoting dimensional quantities. Presenting the solution of Eq. (8) in the form

$$\Omega_z' = \Omega_z'\left[t, z' - (U_\infty\cos\alpha)t, x', y'\right] \quad (9)$$

reduces Eq. (8) to the classical two-dimensional parabolic equation:

$$\frac{\partial\Omega_z'}{\partial t'} + u'\frac{\partial\Omega_z'}{\partial x'} + v'\frac{\partial\Omega_z'}{\partial y'} = \nu\nabla^2_{x,y}\Omega_z' \quad (10)$$

Equation (10) describes the generation of the vorticity along the boundary of the wing (or body) due to the no-slip condition. The generated vorticity is transported and diffused downstream at a velocity $U_\infty\cos\alpha$ (see also Ref. 15). In other words, the solution of Eq. (10) may be obtained in a plane that is advected downstream along the body axis. As a result, the steady flow around slender wings or bodies at incidence can be described by the unsteady, two-dimensional flow development in crossflow planes marching downstream along the body axis, as predicted by the impulsive start flow analogy.[16,17] Equation (10) even extends the domain where the impulsive start flow analogy is applicable by allowing for varying cross-sectional shape while moving along the wing or body axis.

Solution Procedure

Overall Approach

The present solution adopts the ADI method coupled with the vorticity stream function equation, as recommended in Ref. 9. For the purpose, Eq. (10) is rewritten nondimensionally in cylindrical coordinates (r, θ) in the transform plane, using conformal mapping and stream function notation to obtain Eq. (11) for slender delta wings in a nonconservative form:

$$J_0^{-1}\left[\frac{\partial\Omega}{\partial s} - \lambda\frac{\partial b}{\partial\tau}\Omega\right] - \left[\lambda\frac{\partial b}{\partial\tau}r\left(1-\frac{1}{r^4}\right) + \frac{1}{r}\frac{\partial\bar\psi}{\partial\theta} - \frac{\partial\phi}{\partial r}\right]\frac{\partial\Omega}{\partial r} + \frac{1}{r}\left[\lambda\frac{\partial b}{\partial\tau}\frac{2}{r}\sin(2\theta) + \frac{\partial\bar\psi}{\partial r} + \frac{1}{r}\frac{\partial\bar\phi}{\partial\theta}\right]\frac{\partial\Omega}{\partial\theta} = \frac{1}{Re\, b(\tau)}\nabla^2\Omega \quad (11)$$

Where J_0 is the Jacobian of the conformal mapping, $b = b'/b_{max}$, $\Omega = \Omega_z/b(\tau)$, $\bar\psi = \psi/b(\tau)$, $\phi = \bar\phi/b(\tau)$, and s is defined as

$$s = \int_0^\tau \frac{\lambda}{b(\xi)}d\xi \quad (12)$$

The kinematic boundary conditions and the no-slip condition on the wing $(r = r_0)$:

$$\frac{Dr'}{D\tau} = 0, \quad \frac{\partial\bar\psi}{\partial r} = -\frac{1}{r}\frac{\partial\bar\phi}{\partial\theta} \quad (13)$$

and $\bar{\phi}$ is given explicitly as

$$\bar{\phi} = \lambda \frac{\partial b}{\partial \tau} r_0 \left(1 - \frac{1}{r_0^4}\right) \ell n\, r \tag{14}$$

In this particular case, both $\partial_r \bar{\psi}$ *and* $\partial_\theta \bar{\phi}$ at $r = r_0$ are identically zero. Far from the wing, the velocity disturbances must vanish. In general cases, the inner solution for large r is matched to the outer solution in the vicinity of $r \to 0$ by applying the asymptotic matching technique to obtain the free constant $g(z)$ described in Eqs. (5) and (6). In the present study, a delta wing with very small thickness is computed so that $g(z)$ is taken to be zero (similar to the slender-wing assumption).

Expressions for Aerodynamic Coefficients

Some further development of the equations leads to an expression for the pressure on the wing surface in the present case:

$$c_p^* = \frac{2}{Reb(\tau)} \int_0^\theta \frac{\partial \Omega}{\partial r}\, r \mathrm{d}\theta_1 \tag{15}$$

where c_p^* denotes a pressure coefficient defined by a reference pressure on the surface and the crossflow dynamic pressure.

The expression for the normal force coefficient in this case is then obtained as

$$C_N = r_0 \left(r_0 + \frac{1}{r_0}\right) \frac{\sin^2\alpha}{Re} \int_0^1 \int_0^{2\pi} \frac{\partial \Omega}{\partial r} \cos\theta_1 \mathrm{d}\theta_1 \mathrm{d}r \tag{16}$$

where r_0 is the local radius in the transformed plane that represents the wing surface. It should be noted that Eq. (16), obtained for incompressible flow, is identical in its form to the equivalent one presented in Ref. 13, for compressible flow:

$$C_N/\sin^2\alpha = f_1\ (\lambda,\ M_\infty = 0) \tag{17}$$

As pointed out in Ref. 13, it is interesting to compare the Polhamus suction analogy[18] with the results of the present theory. According to the suction analogy, the lift coefficient is given by

$$C_L = K_p \sin\alpha\cos^2\alpha + K_v \sin^2\alpha\cos\alpha \tag{18}$$

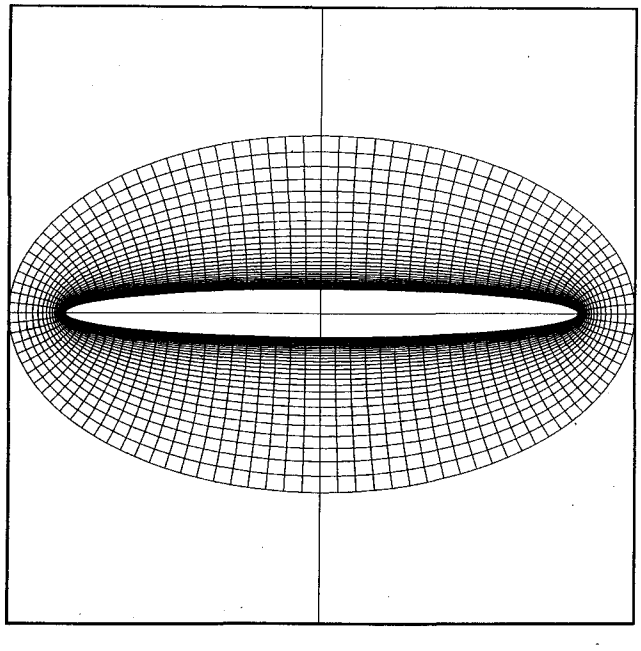

Fig. 2 Example of elliptical cross-section conformal grid.

For slender delta wings, the theoretical values $K_p = \pi AR/2 = 4\pi\lambda\tan\alpha$ and $K_v = \pi$ may be assumed, and so the normal force coefficient takes the form

$$C_N = \pi[4\lambda + 1]\sin^2\alpha \tag{19}$$

Equation 19 is similar in its form to Eq. 16.

Numerical Computation Scheme

The computations are carried out using second-order accuracy in space and first-order accuracy in time. Considering that $\psi^{k+1} = \psi^k + \psi_1$, and $\Omega^{k+1} = \Omega^k + \Omega_1$, where the subscript 1 denotes the correction at time level $k + 1$, then the vorticity equation and the stream function equation can be written in a nonconservative form in the transformed plane[19] as

$$[I + \Delta s A]\,[I + \Delta s C]\,X = f \tag{20}$$

where

$$A = \begin{Bmatrix} \dfrac{v_r^k}{J_0^{-1}}\bar{\delta}_j - \dfrac{1}{ReJ_0^{-1}r_j}\bar{\delta}_j(r_j\bar{\delta}_j), & \dfrac{1}{rJ_0^{-1}}(\bar{\delta}_i\Omega^k)\bar{\delta}_j \\ \dfrac{J_0^{-1}}{\beta}, & -\dfrac{1}{\beta r_j}\bar{\delta}_j(r_j\bar{\delta}_j) \end{Bmatrix} \tag{21}$$

$$C = \begin{Bmatrix} \dfrac{v_0^k}{r_jJ_0^{-1}}\bar{\delta}_i - \dfrac{1}{ReJ_0^{-1}r_j^2}\bar{\delta}_i^2, & \dfrac{1}{r_jJ_0^{-1}}(\bar{\delta}_j\Omega^k)\bar{\delta}_i \\ 0, & -\dfrac{1}{\beta r_j^2}\bar{\delta}_i^2 \end{Bmatrix} \tag{22}$$

$$X = \begin{Bmatrix} \Omega_1 \\ \psi_1 \end{Bmatrix} \tag{23}$$

here, f is the finite difference approximation of Eq. (11) at time level k, whereas v_r^k and v_θ^k are defined as

$$v_r^k = \left[\lambda \frac{\partial b}{\partial \tau} r\left(1 - \frac{1}{r^4}\right) + \frac{1}{r}\bar{\delta}_i\psi - \bar{\delta}_j\phi\right]^k \tag{24a}$$

$$v_\theta^k = \frac{1}{r}\left[\lambda \frac{\partial b}{\partial \tau}\frac{2}{r}\sin(2\theta) + \bar{\delta}_j\psi + \frac{1}{r}\bar{\delta}_i\phi\right]^k \tag{24b}$$

A small streamwise derivative ($\beta\Delta s\,\partial_s\psi$) is added to the stream function equation in order to give it a parabolic type nature, which is necessary for the ADI formulation. The parameter β is chosen arbitrarily. All the partial derivatives have been replaced with their central difference operator, where $\bar{\delta}_i$ and $\bar{\delta}_j$ represent central difference with respect to the r coordinate and the θ direction.

The time step is found to be sensitive to the smallest radius of curvature and also the Reynolds number.

In order to prevent numerical dispersion waves that are typical to central differencing, a first-order upwind difference scheme of the advection can be used; however, this technique tends to smear the results since it introduces an artificial diffusion. On the other hand, a fourth-order artificial viscosity that has been added explicitly has severely reduced the required time step.

A stretched coordinate is used in the radial direction as follows

$$r_j = r_0 \exp\left[\frac{\eta_j - r_0}{2r_0\sqrt{Re}} + \frac{(\eta_j - r_0)^4}{(r_{\max} - r_0)^3}\right] \tag{25}$$

where η_j is evenly spaced in the transform plane and $r_{\max}$ is the maximum computational length that is used. An evenly spaced grid is chosen in the θ direction. An example of the elliptical cross-section conformal grid appears in Fig. 2.

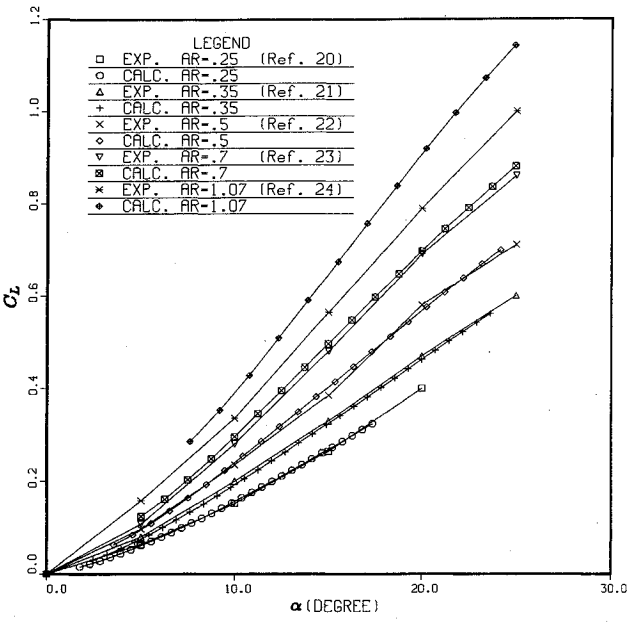

Fig. 3 Lift coefficient of slender delta wings.

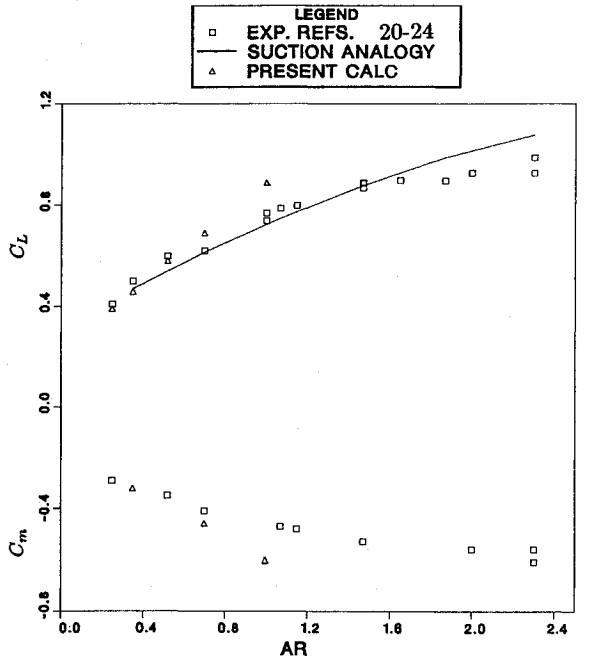

Fig. 4 Lift and pitching moment coefficient vs aspect ratio at $\alpha = 20$ deg.

Results

Aerodynamic Coefficients

The feasibility and accuracy of the present method are tested by computing a series of slender delta wings with aspect ratio of 0.25, 0.35, 0.50, 0.70, and 1.0 in steady incompressible flow, at angles of attack up to 30 deg. For an accurate comparison with experimental data and because the present numerical code has to be modified to include a sharp leading edge, the overall lift and pitching moment coefficients (computed for cross sections having a maximum ellipticity ratio of 10) are first-order extrapolated to an infinite ellipticity ratio (zero leading-edge radius). The extrapolated coefficients are then compared with experimental data for various delta wings having sharp leading edges.[20-24] The variation of the lift coefficient C_L with increasing angle of attack is presented in Fig. 3.

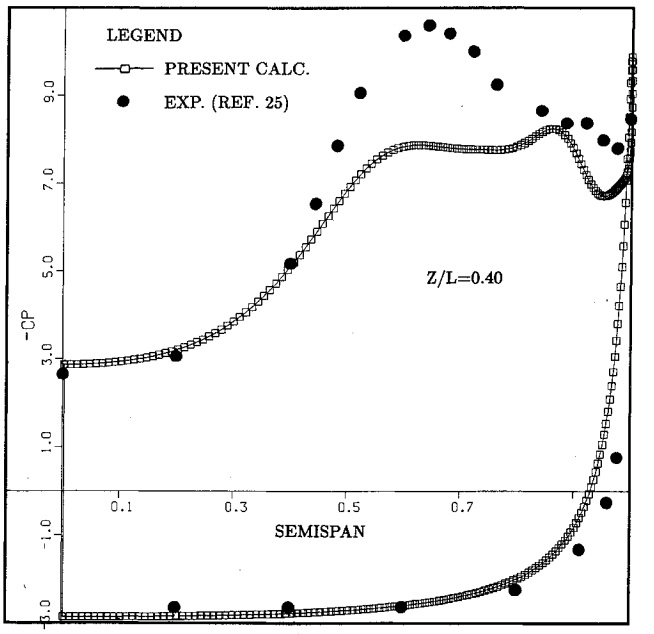

Fig. 5 Surface pressure distribution for $\lambda = 0.33$ ($AR = 0.7$ at $\alpha = 15$ deg).

The calculated results of the present method show an excellent agreement with experimental values for the first four wings, up to an aspect ratio of 0.7, but tend to be higher by about 10% for the $AR = 1$ wing. The difference between the calculated and experimental values in the last case is mainly due to the fact that trailing-edge effect is not included in the present method. As a result, the typical decrease in wing load is not captured there, causing an over-prediction of the lift and pitching moment coefficients. The overprediction is expected to be minor for very slender wings, and becomes more pronounced as the slenderness ratio of the wing decreases (see also Ref. 13). A similar behavior can be seen in Fig. 4, where the variation of lift and pitching moment coefficients with aspect ratio for various delta wings at $\alpha = 20$ deg is shown. The present results for low aspect-ratio wings show a good agreement with experimental data obtained from Refs. 20–24, being also very close to the results computed using the Polhamus suction analogy shown in the same figure. The present results show a deviation from the experimental data as the aspect ratio increases above 0.7.

Pressure Distribution

The first example of the spanwise pressure distribution, computed at $z/L = 0.40$ of a delta wing is presented in Fig. 5, using $\lambda = 0.33$ at $Re = 10^3$ (corresponding to a streamwise Reynolds number of the order of 10^5). Note that the pressure coefficient C_p in Fig. 5 is defined by Eq. (15), using the crossflow dynamic pressure and a reference pressure that is half of the pressure difference between lower and upper wing surface points at its root. A sharp spike of pressure is observed at the leading-edge tip. This spike is typical of slightly rounded leading edges,[22] due to the strong acceleration of the flow around the slightly blunted edge, before its detachment. This pressure spike does not exist in the case of a sharp leading edge. Excluding the edge effect, the main pressure peak in Fig. 5 is due to the effect of the primary vortex. A small secondary peak due to the effect of the secondary vortex is also apparent. The present results underpredict the primary pressure peak when compared with experimental results of Ref. 25, for the same λ, testing a wing of $AR = 0.7$ at $\alpha = 15$ deg and low speed of 80 ft/s. This is possibly due to differences in the exact edge shape and the higher Reynolds number of the experiment. A similar comparison appears in Fig. 6, this time for a

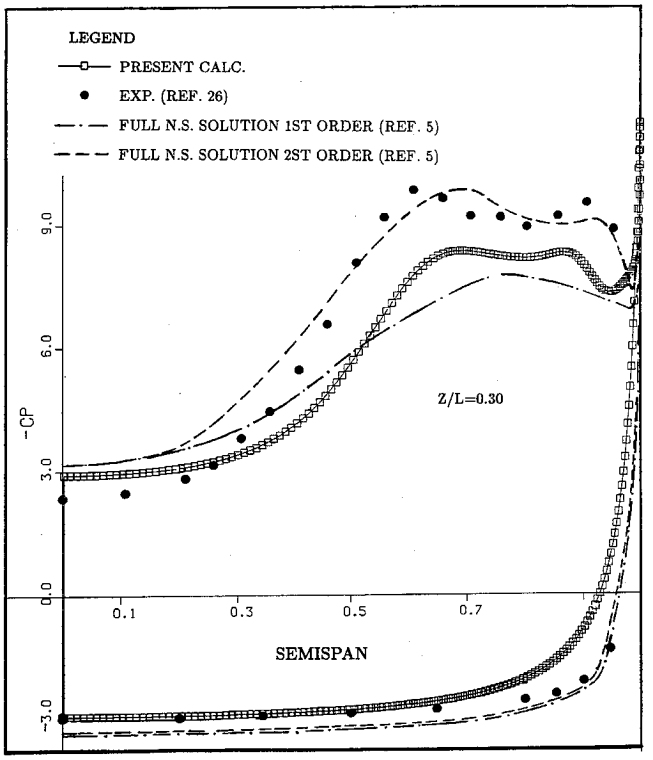

Fig. 6 Surface pressure distribution of $\lambda = 0.33$ ($AR = 1.0$ at $\alpha = 20.5$ deg).

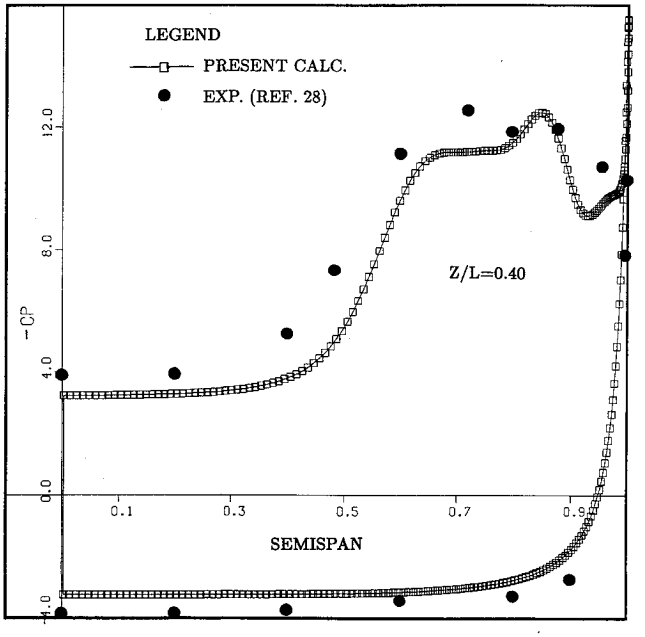

Fig. 7 Surface pressure distribution for $\lambda = 0.50$ ($AR = 0.7$ at $\alpha = 10$ deg).

delta wing having $\lambda = 0.33$ at $z/L = 0.3$, computed also at a chord-based Reynolds number of the order of 10^5. The results are compared with the experimental data of Ref. 26, obtained for a delta wing of $AR = 1$, $\alpha = 20.5$ deg, at a low speed and a chord-based Reynolds number of 9×10^5. Figure 6 also includes the calculated results of the full Navier-Stokes method of Ref. 5 for the same case. The second-order, fine-grid, upwind scheme of Ref. 5, yields the best fit with experimental data on the leeside of the wing. The present method seems to give roughly the same level of comparison as the results of the first-order, fine-grid, upwind scheme of Ref. 5.

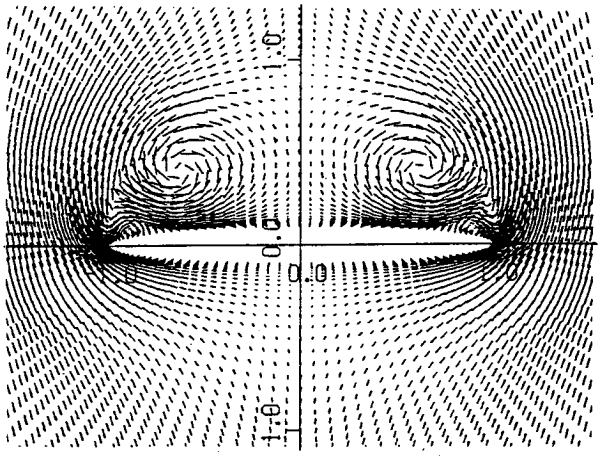

a) Present calculation

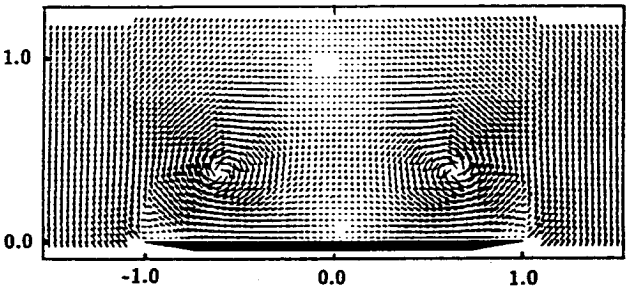

b) Experiment[29]

Fig. 8 Crossflow velocity field for $AR = 1$ delta wing, $z/L = 0.9$ at $\alpha = 20$ deg.

The difference between the present results and the other data close to the leading edge in the windward side is caused by the difference in the cross-section edge shape between the cases. Reference 27 shows that the actual elliptical influence of the trailing edge for this wing becomes significant already at $z/L = 0.5$, and indeed the calculated results of the present method overpredict the experimental data beyond this station, as expected (not shown). A good comparison turns out for the third case, shown in Fig. 7. The calculation is carried out using $\lambda = 0.5$ at $z/L = 0.4$ and at a streamwise Reynolds number of 10^5. Good agreement exists between the computed results and experimental data of Ref. 28, obtained for a delta wing of $AR = 0.7$ at $\alpha = 10$ deg and a low speed of 80 ft/s. The outboard location of the secondary suction peak is typical to the spanwise pressure distribution of delta wings at low Reynolds number.[27]

Crossflow Velocity Field

A typical velocity vector field in the crossflow plane is shown in Figs. 8 for an $AR = 1$ delta wing at $\alpha = 20$ deg and an axial station of $z/L = 0.9$. The calculation is carried out at streamwise Reynolds number of 10^5. The experimental measurements of Ref. 29 for the same wing (at streamwise Reynolds number of 9×10^5) are added to the same figure for qualitative comparison (note the different cross-section shape). The position of the primary vortex core seems to be similar in both cases, but the secondary vortex is more developed in the computed results. The centerline saddle point is evident in both cases at roughly the same height above the wing surface. This figure shows that the present method is capable of capturing very fine details of the flowfield in the crossflow plane.

Vorticity Contours

A sequence of crossflow planes that shows the development of the vorticity contours along the wing appears in Figs. 9a–c at axial stations $z/L = 0.2, 0.53, 0.83$. The computed vorticity contours are obtained for $\lambda = 0.5$, at a crossflow Reynolds number $Re = 10^3$, using a time step of $\min(J_0^{-1})/100$ and a mesh of 60 grid points in the radial direction and 108 points in the circumferential direction (half plane).

In Fig. 9a ($z/L = 0.2$), the primary vortex is not yet fully developed and it lies close to the wing surface, with signs of a secondary vortex staring to emerge from the surface. Following the evolution of the flow along the wing axis, Fig. 9b ($z/L = 0.53$) shows that the primary vortex at this station is much more developed, moving up and occupying a larger part of the wing span. The secondary vortex at this station is stronger and larger in size, clearly affecting the separated shear layer that feeds the primary vortex. The interaction between the secondary and the primary vortices is caused by viscous effects (shear and entrainment of the fluid particles). As a result, the primary vortex feeding sheet gets thicker, losing some of its momentum, and possible becoming less stable. Some fluid entrainment also occurs between the already rolled-up primary vortex sheet and the secondary vortex. Traces of a possible weak tertiary vortex appear in Figs 9b and 9c, just beneath the secondary vortex. Figure 9c further describes the development of the vortex flow in the crossflow plane, at $z/L = 0.83$, with essentially the same features that appear in Fig. 9b. The wavy disturbance in the primary vortex outer contour line in Figs 9c is probably the result of insufficient grid resolution in this region of the flow. It should be noted that the description of the flow phenomena appears to be more sensitive and informative using vorticity contours instead of classical stream function contours. Figures 10 show the experimentally measured vorticity contours obtained by Ref. 29 for a 75 deg delta wing at $\alpha = 20.5$ deg and a chordwise Reynolds number of 10^6, at $z/L = 0.7$. The present calculated results shown in the same figure capture the flow details, including secondary separation and its influence on the primary shear layer.

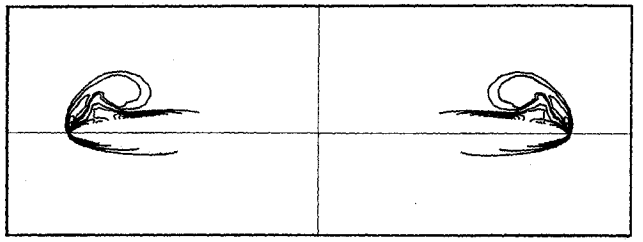

a) $z/L = 0.20$

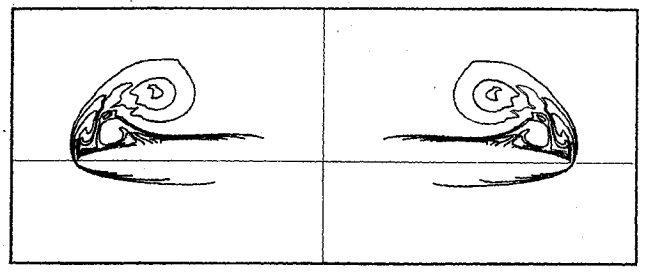

b) $z/L = 0.533$

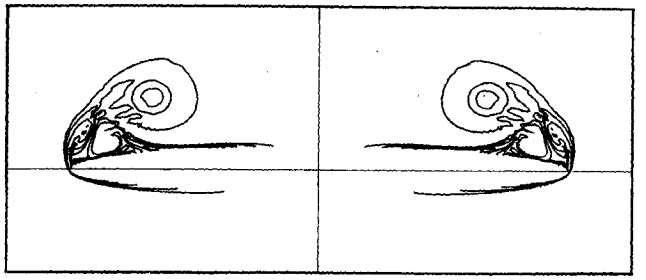

c) $z/L = 0.866$

Fig. 9 Chordwise development of crossflow iso-vorticity contours, $\lambda = 0.5$, $Re = 10^3$

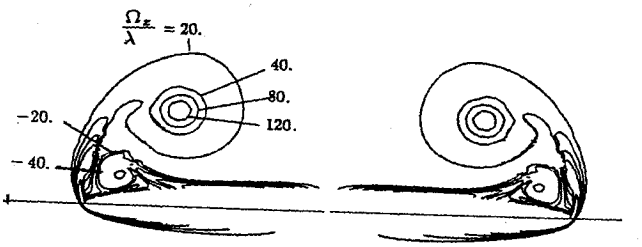

a) Present calculation

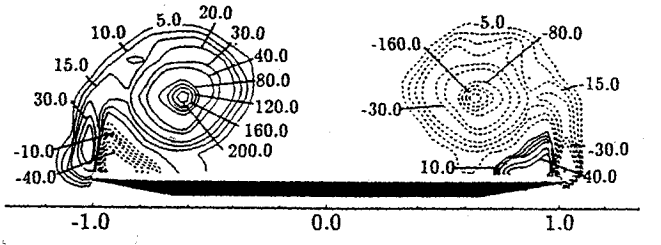

b) Experiment[29]

Fig. 10 Crossflow iso-vorticity contours, 75 deg delta wing at $\alpha = 20.5$ deg, $z/L = 0.7$.

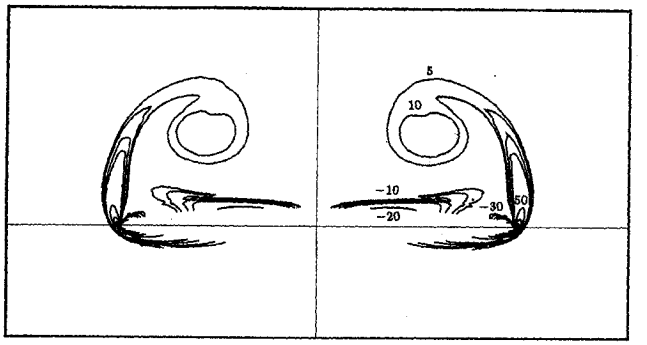

a)

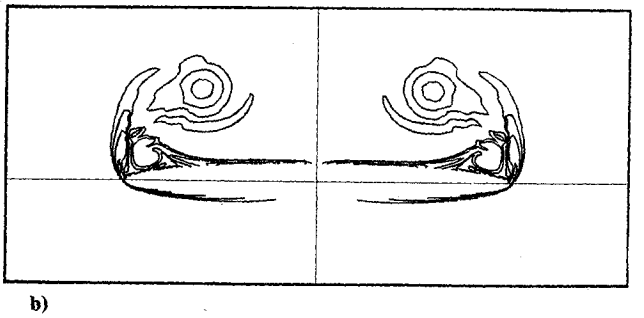

b)

Fig. 11 Crossflow iso-vorticity contours at two different crossflow Reynolds numbers, $\lambda = 0.25$, $z/L = 0.99$.

Figures 11 show an example of the vorticity contours obtained at $z/L = 0.99$, for $\lambda = 0.25$ and crossflow Reynolds number of $Re = 10^2$ (Fig. 11a) and 10^3 (Fig. 11b). Both cases show a well-developed primary vortex. As explained in the previous case, the higher Reynolds number calculation suffers probably from insufficient grid density in the primary vortex region, as appears from Fig. 11b. The Reynolds number seems to affect the location and development of the secondary vortex. It is clear that the secondary vortex in Fig. 11b, calculated at $Re = 10^3$, is much more developed than the one in Fig. 11a, calculated at $Re = 10^2$. It also seems that the secondary vortex obtained at $Re = 10^2$ is located more inboard than the one obtained at $Re = 10^3$.

Conclusions

The new computational method can be used to calculate the flow about slender wing or body shapes. Accurate results are obtained as long as the basic slenderness assumption is met. The theory developed supports the impulsive start flow analogy as a valid approximation for slender body vortical flow, while extending the computational domain to more complex geometries as well. The present theory arrives at an expression for the lift coefficient, which is very similar to the one derived in the Polhamus suction analogy for delta wings. The parabolization of the problem in the inner, viscous flow domain makes the new method very attractive to use for solving incompressible or subsonic flow cases, due the fast plane-marching scheme it employs. The new method shows high sensitivity in capturing flow phenomena such as primary and secondary vortex separation, roll-up, and mutual interaction. The vorticity equation formulation used in the present method offers good insight into, and convenient physical interpretation of, the flow.

The present calculations prove the feasibility of the new method while applying some simplifying assumptions to the flow model. One of the assumptions, namely, neglecting the axial velocity gradient within the thin boundary-layer zone on the wing surface, could be removed to obtain a more accurate model. Such a model would describe the mechanism of smooth surface separation more exactly, thus improving the prediction of secondary separation on delta wings and also allowing for wider domain of geometries to be calculated. Future studies should include an effort to calculate the elliptic influence of the trailing edge on the pressure field upstream. Further development should also include topics such as compressible flow (see Ref. 13), unsteady flow, and asymmetric flow cases.

References

[1]Rizzi, A., and Muller, B., "Large-Scale Viscous Simulation of Laminar Vortex Flow over a Delta Wing," *AIAA Journal*, Vol. 27, No. 7, 1989, pp. 833-840.

[2]Kandil, O. A., and Chuang, A. H., "Influence of Numerical Dissipation on Computational Euler Equations for Vortex-Dominated Flows," *AIAA Journal*, Vol. 25, No. 11, 1987, pp. 1426-1434.

[3]Pulliam, T. H., "Euler and Thin Layer Navier-Stokes Codes: Arc2d, Arc3d" *Notes for Computational Fluid Dynamics*, University of Tennessee Space Institute, Tullahoma, TN, March, 1984 (unpublished material).

[4]Fujii, K., Gavali, S., and Holst, L. T., "Evaluation of Navier-Stokes and Euler Solution for Leading-Edge Separation" *International Journal for Numerical Methods in Fluids*, Vol. 8, No. 10, 1988, pp. 1319-1329.

[5]Hartwich, P.M., Hsu, C. H., and Liu, C. H., "Vectorizable Implicit Algorithms for the Flux-Difference Split, Three-Dimensional Navier-Stokes Equations," *Journal of Fluids Engineering*, Vol. 110, Sept. 1988, pp. 297-305.

[6]Hsu C. H., Hartwich, P. M., and Liu, C. H., "Three-dimensional Incompressible Navier-Stokes Simulations of Slender-Wing Vortices," AIAA Paper 87-2476, Aug. 1987.

[7]Fujii, K, and Schiff, L. B., "Numerical Simulation of Vortical Flows over a Strake-Delta Wing," *AIAA Journal*, Vol. 27, No. 9, 1989, pp. 1153-1162.

[8]Khosla, P. K., and Lai, H. T., "Global PNS Solutions for Subsonic Strong Interaction Flow over a Cone-Cylinder-Boattail Configuration," *Computers & Fluids*, Vol. 11, No. 4, 1983, pp. 325-339.

[9]Briley, W.R., and McDonald, H. "Three Dimensional Viscous Flows with Large Secondary Velocity," *Journal of Fluid Mechanics*, Vol. 144, 1984, pp. 47-77.

[10]Sychev, V. V., "Three-Dimensional Hypersonic Gas Flow Past Slender Bodies at High Angles of Attack," *Prikladnaia Matematika i Mekhanika*, Vol. 24, No. 2, 1960, pp. 205-212.

[11]Barnwell, R. W., "Extension of Hypersonic, High-Incidence, Slender-Body Similarity," *AIAA Journal*, Vol. 25, No. 11., 1987, pp. 1519-1522.

[12]Hemsch, M. J., "Engineering Analysis of Slender-Body Aerodynamics Using Sychev Similarity Parameters," *Journal of Aircraft*, Vol. 25, No. 7, 1988, pp. 625-631.

[13]Hemsch, M. J., "Similarity for High-Angle-of-Attack Subsonic/Transonic Slender-Body Aerodynamics," *Journal of Aircraft*, Vol. 26, No. 1, 1989, pp. 56-66.

[14]Nielsen, J. N., "Missile Aerodynamics," Nielsen Engineering & Research, Inc., Mountain View, CA 1988.

[15]McCune, J. E., Tavares, T. S., Lee, N. K. W., and Weissbein, D., "Slender Wing Theory Including Regions of Embedded Total Pressure Loss," AIAA Paper 88-0320, Jan. 1988.

[16]Allen, J. H., and Perkins, E. W., "Characteristics of Flow over Inclined Bodies of Revolution," NACA RM A50L07, March 1951.

[17]Sarpkaya, T., "Separated Flow About Lifting Bodies and Impulsive Flow About Cylinders," *AIAA Journal*, Vol. 4, No. 3, 1966, pp. 414-420.

[18]Polhamus, E. C., "Prediction of Vortex-Lift Characteristics by a Leading-Edge Suction Analogy," *Journal of Aircraft*, Vol. 8, No. 4, 1971, pp. 193-199.

[19]Beam, R. M., and Warming, R. F., "An Implicit Finite Difference Algorithm for Hyperbolic Systems in Conservation-Law Form," *Journal of Computational Physics*, Vol. 22, No. 1, 1976, pp. 87-110.

[20]Fox, C. H., and Lamar, J. E., "Theoretical and Experimental Longitudinal Aerodynamic Characteristics of an Aspect Ratio 0.25 Sharp-Edge Delta Wing at Subsonic, Supersonic and Hypersonic Speeds," NASA TN D-7651, Aug. 1974.

[21]Wentz, W. H., Jr, and Kohlman, D. L., "Vortex Breakdown on Slender Sharp-Edged Wings," *Journal of Aircraft*, Vol. 8, No. 3, 1971, pp. 156-161.

[22]Bartlet, G. E., and Vidal, R. J., "Experimental Investigation of the Influence of Edge Shape on the Aerodynamic Characteristics of Low Aspect Ratio Wings at Low Speeds," *Journal of Aeronautical Sciences*, Vol. 22, Aug. 1955, pp 517-533.

[23]Fink, P. T., "Wind-Tunnel Tests on a Slender Delta Wing at High Incidence," *Zeitschrift fur Flugwissenschaften*, Jahrg. 4, Heft 7, July 1956, pp. 247-249.

[24]Peckham, D. H., "Low-Speed Wind Tunnel Tests on a Series of Uncambered Slender Pointed Wings with Sharp Edges," A.R.C RM 3186, 1961.

[25]Harvey, J. K., "Some Measurements on a Yawed Slender-Delta Wing with Leading-Edge Separation," British A.R.C. 20451, Oct. 1958.

[26]Hummel, D., "Zur Umstromung Scharfkantiger Schlanker Deltaflugel bei groben Anstellwinkeln," *Z. Flugwiss*, Vol. 15, 1967, pp. 376-385.

[27]Hummel, D., "Documentation of Separated Flows for Computational Fluid Dynamics Validation," AGARD CP-437, May 1988.

[28]Fink, P. T., "Further Experiments with 20 deg. Delta Wings," British A.R.C. 19526, Sept. 1957.

[29]Kjelgaard, S. O., and Sellers, W. L., "Detailed Flowfield Measurements over a 75° Swept Delta Wing for Code Validation," AGARD CP-437, May 1988.